

SUPPLEMENTAL MATERIAL

Evidence for a lithospheric step and pervasive lithospheric thinning beneath southern New England by G. Goldhagen et al.

Sp receiver function analysis and common conversion point stacking methodology

Waveform data were downloaded from the IRIS Data Management Center (DMC). All data to be used in the study are open access, including SEISConn data. Sp waveforms were limited to events at epicentral distances of 55°-85°, magnitudes of 5.8 or greater and depths of less than 300 km. Waveform preprocessing included rotation into the radial and transverse components and bandpass filtering. Predicted S-wave arrival times were estimated by using the 1D velocity model, AK315 (Kennett et al., 1995), and the TauP ray tracing program (Crotwell et al., 1999). The predicted arrival times were compared to estimated arrival times based on signal to noise analysis (S2N). Our S2N analysis follows the methodology described in detail in Abt et al. (2010) (Section 3.1 Phase Picking). Briefly, we use the short-term-average to long-term-average moving window method of Earle and Shearer (1994), using a signal window length of 10 seconds and a noise window length of 40 seconds. The S2N ratio of the envelope function was then generated for a range of ± 25 seconds around the TauP predicted phase arrival. If the TauP predicted- and S2N estimated arrival times were greater than 5 seconds apart, the waveform was discarded all other data were used and no other metrics were used for culling. The number of events requested versus the number of events used in the final analysis varied from network and network and station to station. For example, 210 waveforms were downloaded from the IRIS DMC for station L64A (N4), of which 74 were culled. 145 waveforms were downloaded for station CS08 (XP; SEISConn) and 65 were culled. 251 were downloaded for station LSCT (US), and 99 were culled. A full list of downloaded events and culled events are available per station in Table DR1. Waveforms were then rotated into the P-SV-SH reference frame using a best-fitting free-surface transform (Bostock, 1998). The parameters for the free-surface transform were determined through an automated procedure detailed in Abt et al. (2010). This involves the parent phase (SV) being windowed around its arrival time, and a search performed over a range of V_p and V_p/V_s to find the values that minimized the correlation of the parent phase with a corresponding window on the daughter component (P). For each station all cross-correlation surfaces with well-defined minima were stacked and the best free surface velocities for the individual station were defined as the minimum of this stack.

After waveform preprocessing, receiver functions were calculated using an extended time multitaper (ETMT) deconvolution technique (Helffrich, 2006) and bandpass filtered between 2-100 s. An additional filter of 2-33 s was initially tried but resulted in results with less coherence. Our preferred filter is similar to the one applied in Hopper and Fischer (2018) and tested in Mancinelli et al. (2017), both of which used the same receiver function code. The polarity of the

Sp receiver functions were reversed to match the typical Ps convention. Receiver function time series were migrated to depth using the crustal velocity model Crust1.0 (Laske et al., 2013) and the regional 3D seismic tomography model for mantle velocities (Schmandt & Lin 2014, Schmandt et al., 2015). We utilize the model of Schmandt and Lin (2014) for P-wave velocities at all mantle depths, and S-wave velocities below 120 km, and Schmandt et al. (2015) for S-wave velocities above 120 km. To incorporate 3D structure while avoiding numerically intensive ray tracing, a 1D model was generated for each point in latitude/longitude space, averaging the 3D model at each depth according to the size of the predicted Fresnel zone, similar to what has been done in previous Sp receiver function studies. This 1-D average is then applied to each station-event pair for a given station. (Lekic et al., 2011; Ford et al., 2014; Hopper and Fischer, 2015; Hopper et al, 2017; Hopper and Fischer, 2018). Uncertainties associated with utilizing an incorrect migration model in our analysis are discussed in the supplementary materials of Lekic et al (2011). Using synthetics, Lekic et al (2011) argue that uncertainties do not exceed 5 km and are likely less than that.

The migrated Sp receiver functions were stacked in a 3D model discretized at 0.1° increments in latitude and longitude, and 0.5 km in depth. A weighted average of individual receiver functions was calculated, with weights given by cubic spline functions that approximate the Sp phase Fresnel zone (Lekic et al., 2011). In order to place constraints on the uncertainties in depth and amplitude, the finalized CCP migrated receiver functions were calculated using an iterative bootstrapping technique (Hopper and Fischer, 2018).

Negative phase interpretation

Side lobes are a demonstrated artifact of Sp receiver function analysis, and more specifically receiver functions calculated using the extended time multitaper technique used here (Lekic and Fischer, 2017). To minimize the appearance of side-lobes, we perform windowing in the time domain before deconvolution to exclude post-S arrivals and filter to sufficiently high frequencies (0.5 Hz), two techniques that have been documented to reduce the appearance of side lobes (Lekic and Fischer, 2017). Qualitatively, we observe that our interpreted phase does not consistently track with the positive phase energy at shallower depths (Moho), which would be indicative of a side lobe phase. For example, in cross section D-D' from a longitude of $\sim 75^\circ\text{W}$ to $\sim 73.2^\circ\text{W}$ the positive phase (i.e., Moho) shallows considerably while the negative phase remains flat. Conversely, in cross section B-B' the positive phase remains flat across the study region. A side lobe would track with the Moho phase, in contrast to what we see.

Demonstrating a difference in negative phase depth and amplitude across the terrane boundary

In order to facilitate an understanding of how robust the change in depth and amplitude of the selected negative phase is across the Taconic belt/Ganderia terrane boundary, we examined both

the distribution of data using histograms and through the use of kmeans clustering analysis. Initial histograms plots were made with the raw depth and amplitude values in our study area, for regions west and east of the terrane boundary (Figures DR3 & DR4). While a robust calculation of the mean and standard deviation is not possible given the multimodal distribution of depths, which appear to correlate with real changes in structure, we do calculate average values for both populations and find average values of depth west of the boundary to be 80 km, east of the boundary 66 km, and amplitudes west of the boundary to be 0.11 and east of the boundary 0.08. To better understand the relationship between amplitude, depth and terrane boundary we again divided our results into two groups according to whether they are west or east of the terrane boundary (Figure DR3), and then compared these results to data divided using kmeans clustering analysis, in which the only variables are depth and amplitude. In our comparison we find that 81% of the points divided into the terrane groupings agree with the groups determined by kmeans analysis, assuming that only two clusters are used. The remaining 19% of the points disagree, and primarily fall in a region of overlap at ~60 to ~75 km (Figure DR5).

Is the negative phase a mid-lithospheric discontinuity or the lithosphere-asthenosphere boundary?

The negative phases selected in our study are thought to represent a negative velocity gradient associated with the transition from high seismic velocity lithosphere to low seismic velocity asthenosphere. Using a framework developed previously (Abt et al., 2010; Ford et al., 2010; Birkey et al., 2021), we define the lithosphere as being the depth range in which a positive velocity gradient (increasing velocity with increasing depth) is present, starting beneath the crust and extending until a local maximum is reached. The potential lithosphere-asthenosphere boundary depth range begins at this peak in absolute velocity and ends when a minimum in absolute velocity (thought to be indicative of the asthenosphere) is reached. The absolute velocities used in this study come from the ambient noise tomography model of Yang and Gao (2018).

To best illustrate the correspondence between our negative phase picks and the tomography model, we averaged the velocity model according to latitude, into two groups (Figure 4 of main text). The averaged models were then used to determine our potential LAB depth range (magenta lines). We plotted our negative phase picks within each averaged region, shading them according to their location in latitude. For the 42.1-43°N averaged region, where the lithospheric step is less pronounced according to receiver functions, the LAB phases fall almost entirely within or below the potential LAB depth range. For the 41.2-42°N averaged region, where the lithospheric step is more abrupt, the LAB phases typically fall within or below the potential LAB depth range. However, a few potential LAB phases in the local maximum (solid magenta line) step down at ~72°W, while our receiver functions imply that a flatter LAB is present.

Supplemental Material Figure and Table Captions

Table S1. Full table of station names, events with data per each station, and events culled due to low signal-to-noise ratios.

Figure S1. (a) Original cross sections shown in Figure 2 of the main text; alongside (b) the sampling density, which is determined by the number of weighted events using the Sp Fresnel zone approximation discussed in the data repository; and (c) two standard deviation of the bootstrapped receiver functions. Note the dearth of data at 150-200km from 75-72.5°W. Terrane boundaries are shown at the top of (b) profiles and correspond in color to the terranes in Figures 1 and 2 of the main text.

Figure S2. Map view of sampling density, shown for a depth slice at 70km, which is determined by the number of weighted events using the Sp Fresnel zone approximation discussed in the data repository.

Figure S3. Map illustrating how individual points within the receiver function model were subdivided in order to determine average depth and amplitude of the negative phase east and west of the Taconic-Ganderia Boundary, generate histograms (Figure DR4) and in the clustering comparison (Figure S5)

Figure S4. Histograms of negative phase depth (top row) and amplitude (bottom row) for negative phases located west (left column) and east (right column) of the Taconic-Ganderia boundary.

Figure S5. (top) Negative phase picks grouped by terrane and plotted as a function of amplitude vs depth. Red points correspond to negative phases located east of the terrane boundary (Figure S3) and blue points correspond to negative phases located to the west of the terrane boundary (Figure S3). (middle) Negative phase picks clustered according to kmeans analysis, assuming that only two clusters are used. No prior knowledge of point locations are known during kmeans analysis and colors are randomly assigned and do not correspond to colors shown in the top panel. (bottom) Comparison of the kmeans clustering methodology relative to grouping based on location relative to the terrane boundary. Grey points mark points that agree between the two methods while pink points mark the 19% of points that disagree.

References:

Abt D.L. Fischer K.M. French S.W. Ford H.A. Yuan H. Romanowicz B., 2010, North American lithospheric discontinuity structure imaged by Ps and Sp receiver functions: *Journal of Geophysical Research* , v. 115, B09301, doi:10.1029/2009JB006914.

Birkey A. Ford H.A. Dabney P. Goldhagen G., 2021, The lithospheric architecture of Australia from seismic receiver functions: *Journal of Geophysical Research: Solid Earth*, 126(4), p.e2020JB020999.

Bostock, M.G., 1998, Mantle stratigraphy and evolution of the Slave province: *Journal of Geophysical Research* , v. 103p. 21183-21200.

Crotwell, H.P., Owens, T.J., and Ritsema, J., 1999, The TauP toolkit: Flexible seismic travel-time and ray-path utilities: *Seismological Research Letters* , v. 70, p. 154–160, <https://doi.org/10.1785/gssrl.70.2.154>.

Ford, H.A., Fischer, K.M., Abt, D.L., Rychert, C.A., and Elkins-Tanton, L.T., 2010, The lithosphere-asthenosphere boundary and cratonic lithospheric layering beneath Australia from Sp wave imaging: *Earth and Planetary Science Letters*, v. 300, p. 299–310, doi:10.1016/j.epsl.2010.10.007.

Ford, H.A., Fischer, K.M., and Lekic, V., 2014, Localized shear in the deep lithosphere beneath the san andreas fault system: *Geology*, v. 42, p. 295–298, doi:10.1130/G35128.1.

Helffrich G., 2006, Extended-time multi-taper frequency domain cross-correlation receiver function estimation: *Seismological Society of America Bulletin* , v. 96, p. 344–347, doi:10.1785/0120050098.

Hopper, E., and Fischer, K.M., 2015, The meaning of midlithospheric discontinuities: A case study in the northern U.S. craton: *Geochemistry, Geophysics, Geosystems*, v. 16, p. 4057–4083, doi:10.1002/2015GC006030.

Hopper, E., and Fischer, K.M., 2018, The changing face of the lithosphere-asthenosphere boundary: Imaging continental scale patterns in upper mantle structure across the contiguous US with Sp converted waves: *Geochemistry Geophysics Geosystems* , v. 19, p. 2593–2614, <https://doi.org/10.1029/2018GC007476>.

Hopper, E., Fischer, K.M., Wagner, L.S., and Hawman, R.B., 2017, Reconstructing the end of the Appalachian orogeny: *Geology*, v. 45, p. 15–18, doi:10.1130/G38453.1.

Kennett, B.L.N., Engdahl, E.R., and Buland, R., 1995, Constraints on seismic velocities in the Earth from travel times: *Geophysical Journal International* , v. 122, p. 108–124, <https://doi.org/10.1111/j.1365-246X.1995.tb03540.x>.

Laske, G., Masters, G., Ma, Z., and Pasyanos, M.E., 2013, Update on CRUST1.0: A 1-degree global model of Earth's Crust: *Geophysical Research Abstracts* , v. 15, Abstract EGU2013–2658.

Lekic V. French S.W. Fischer K.M., 2011, Lithospheric thinning beneath rifted regions of southern California: *Science* , v. 334, p. 783–787, doi:10.1126/science.1208898.

Mancinelli, N.J., Fischer, K.M., and Dalton, C.A., 2017, How Sharp Is the Cratonic Lithosphere-Asthenosphere Transition? *Geophysical Research Letters*, v. 44, p. 10,189-10,197, doi:10.1002/2017GL074518.

Schmandt, B., and Lin, F.C., 2014, P and S wave tomography of the mantle beneath the United States: *Geophysical Research Letters*, v. 41, p. 6342–6349, doi:10.1002/2014GL061231.

Schmandt, B., Lin, F.C., and Karlstrom, K.E., 2015, Distinct crustal isostasy trends east and west of the Rocky Mountain Front: *Geophysical Research Letters*, v. 42, p. 10290–10298, doi:10.1002/2015GL066593.

Yang, X., and Gao, H., 2018, Full-Wave Seismic Tomography in the Northeastern United States: New Insights Into the Uplift Mechanism of the Adirondack Mountains: *Geophysical Research Letters*, v. 45, p. 5992–6000, doi:10.1029/2018GL078438.

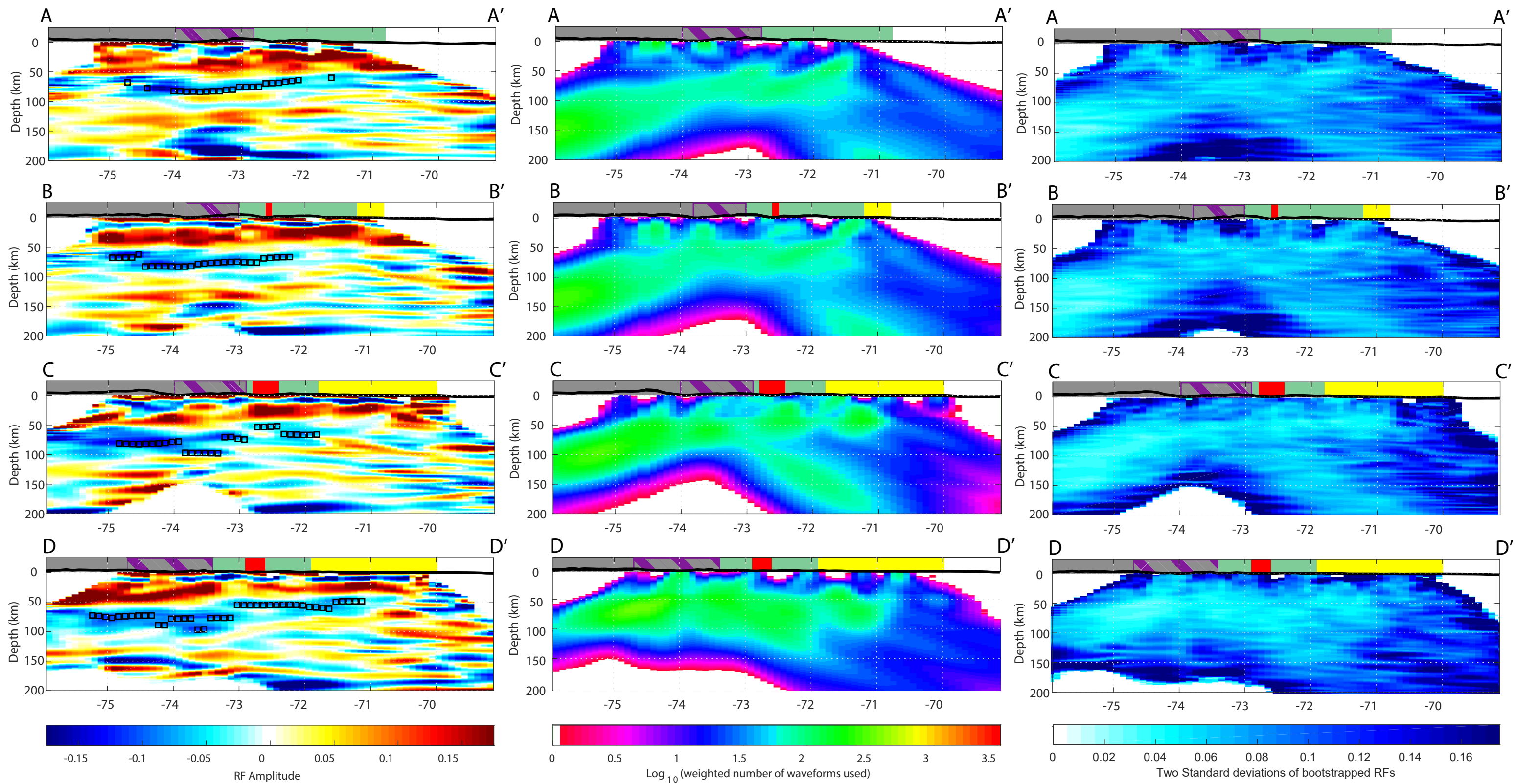


Figure DR1. (a) Original cross sections shown in Figure 2 of the main text; alongside (b) the sampling density, which is determined by the number of weighted events using the Sp Fresnel zone approximation discussed in the data repository; and (c) two standard deviation of the bootstrapped receiver functions. Note the dearth of data at 150-200km from 75-72.5°W. Terrane boundaries are shown at the top of (b) profiles and correspond in color to the terranes in Figures 1 and 2 of the main text.

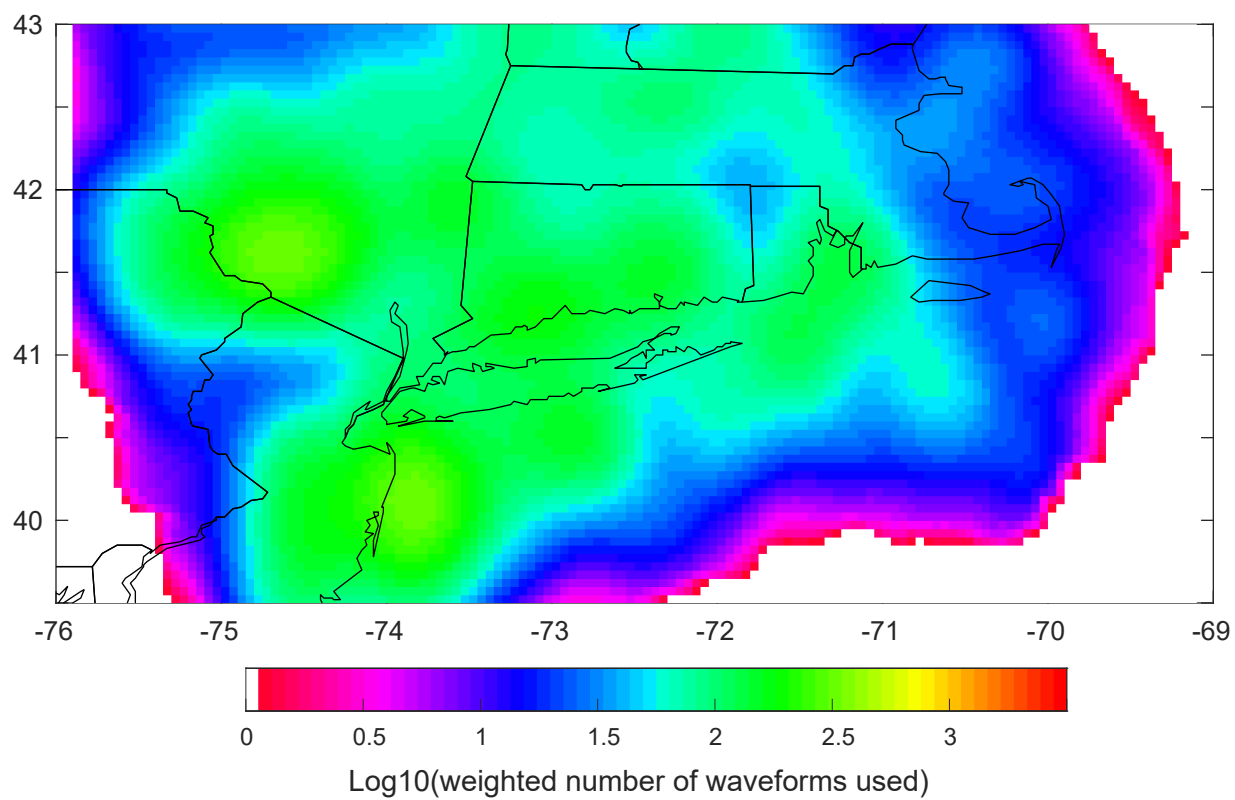


Figure DR2. Map view of sampling density, shown for a depth slice at 70km, which is determined by the number of weighted events using the Sp Fresnel zone approximation discussed in the data repository.

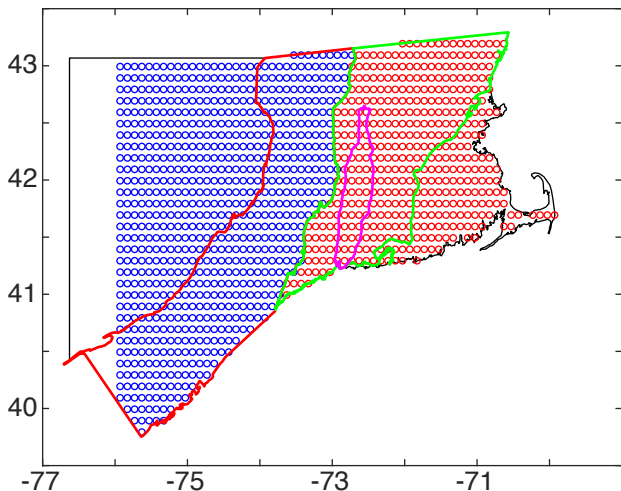


Figure DR3. Map illustrating how individual points within the receiver function model were subdivided in order to determine average depth and amplitude of the negative phase east and west of the Taconic-Ganderia Boundary, generate histograms (Figure DR4) and in the clustering comparison (Figure DR5)

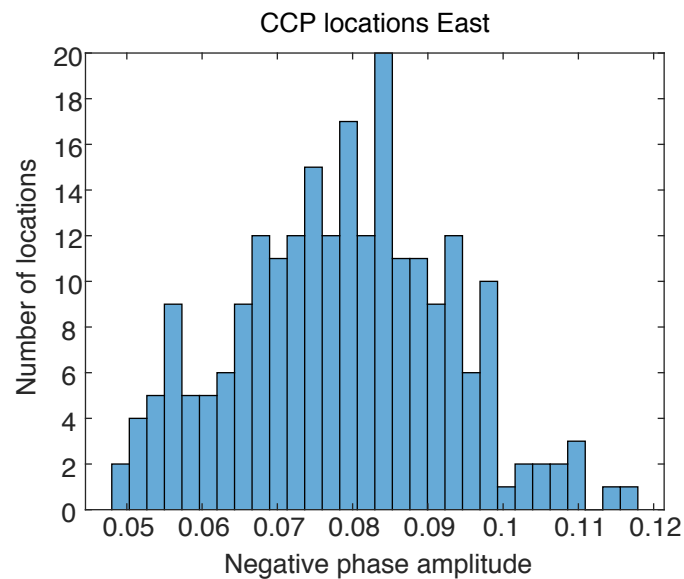
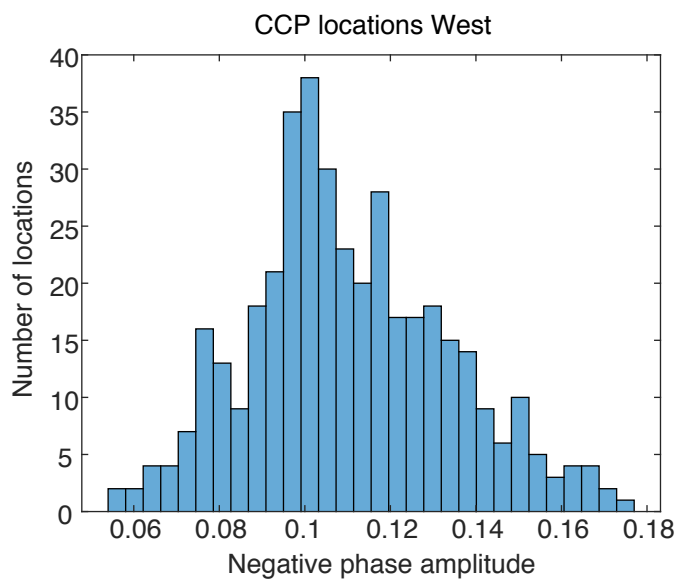
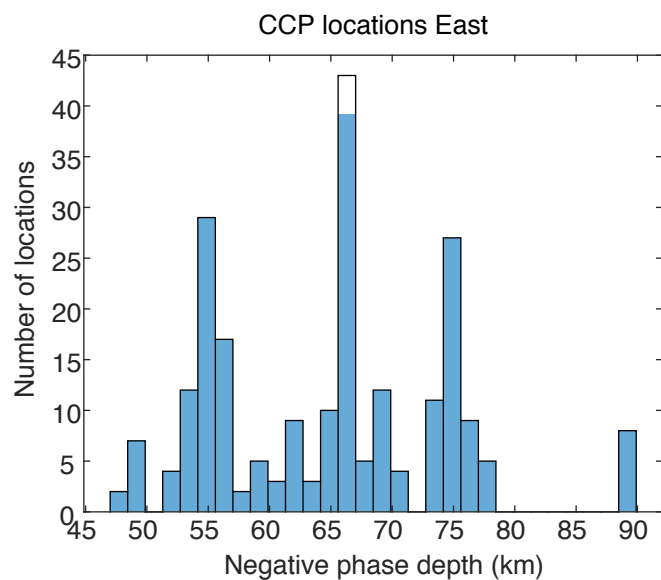
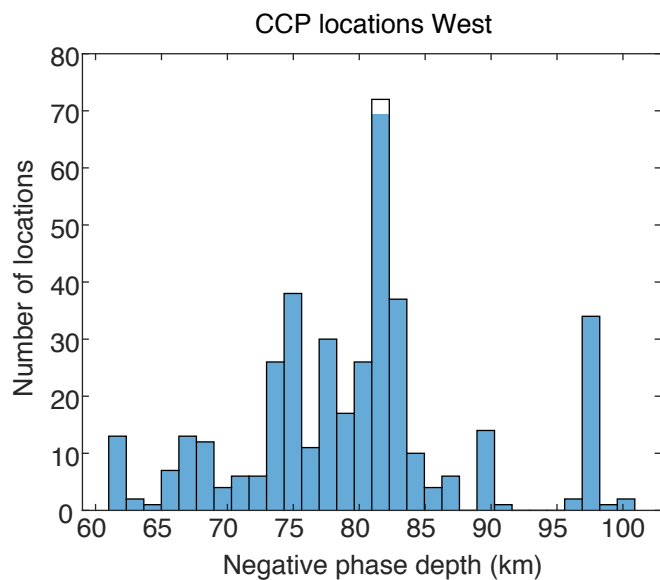


Figure DR4. Histograms of negative phase depth (top row) and amplitude (bottom row) for negative phases located west (left column) and east (right column) of the Taconic-Ganderia boundary.

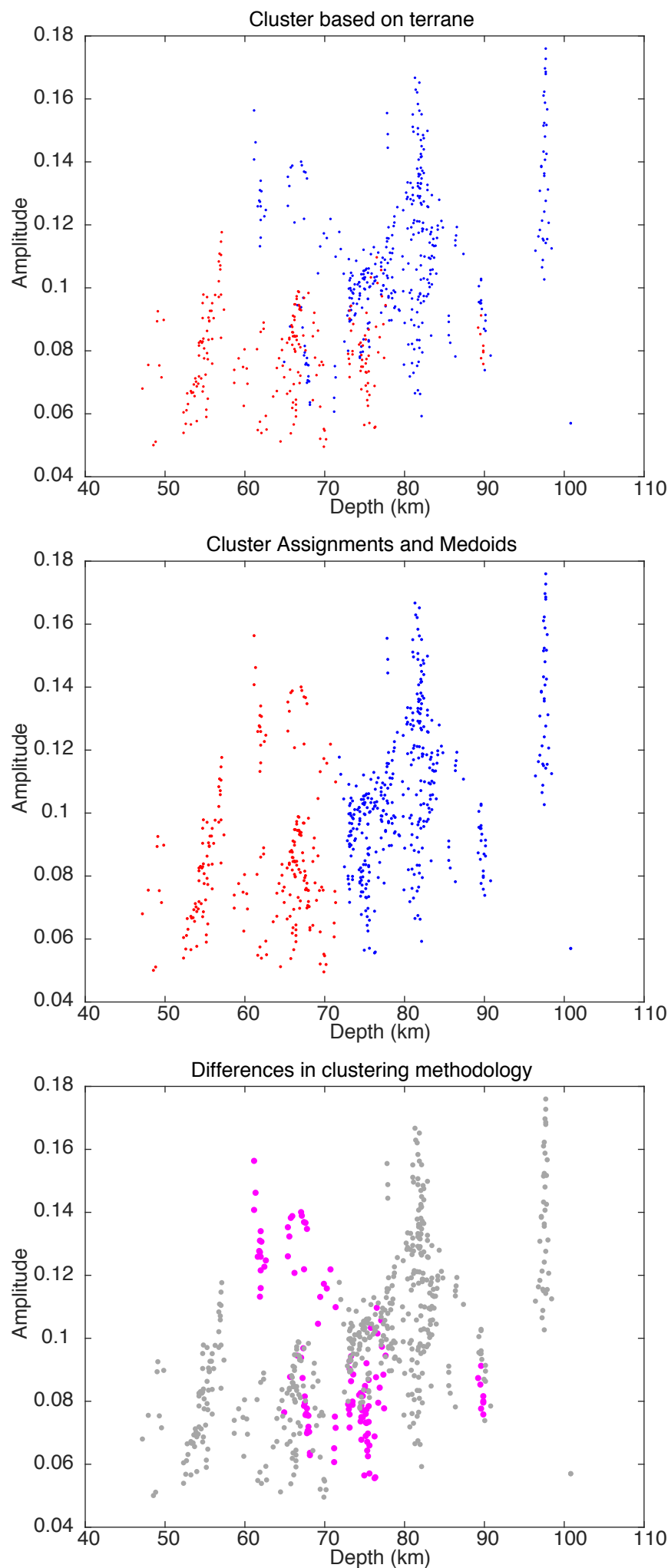


Figure DR5. (top) Negative phase picks grouped by terrane and plotted as a function of amplitude vs depth. Red points correspond to negative phases located east of the terrane boundary (Figure DR3) and blue points correspond to negative phases located to the west of the terrane boundary (Figure DR3). (middle) Negative phase picks clustered according to kmeans analysis, assuming that only two clusters are used. No prior knowledge of point locations are known during kmeans analysis and colors are randomly assigned and do not correspond to colors shown in the top panel. (bottom) Comparison of the kmeans clustering methodology relative to grouping based on location relative to the terrane boundary. Grey points mark points that agree between the two methods while pink points mark the 19% of points that disagree.